Available online at www.sciencedirect.com

ScienceDirect

IFAC PapersOnline CONFERENCE PAPER ARCHIVE

IFAC PapersOnLine 58-5 (2024) 66–71

Enabling Tunability of a MEMS Sensor with a Geometric Nonlinearity [1]

Hermann Folke Johann Rolf * **Thomas Meurer** *

* *Digital Process Engineering Group, Institute of Mechanical Process Engineering and Mechanics, Karlsruhe Institute of Technology, Hertzstr. 16, D-76187 Karlsruhe, Germany (e-mail {folke.rolf, thomas.meurer}@kit.edu).*

Abstract: The properties of a thermally actuated MEMS sensor with a geometric nonlinearity are investigated. This MEMS sensor is a potential candidate to construct a neuromorphic acoustic sensor to mimic the functionality of the cochlea by controlling an Andronov-Hopf bifurcation with the thermal actuator. The resonance frequency of this sensor becomes tunable by introducing a geometric nonlinearity. With this nonlinearity the frequency response of the neuromorphic acoustic sensor is controllable by assigning a DC-voltage. Moreover, the effects of harmonic excitation on the MEMS sensors are analyzed. Here, the critical points of saddle-node bifurcations are approximated and the movement of the frequency with respect to a harmonic excitation is discussed. The results are illustrated by numerical simulations.

Keywords: Andronov-Hopf bifurcation, saddle-node bifurcation, MEMS sensor, Duffing equation, Tunability, Neuromorphic acoustic sensing, Neuromorphic engineering

1. INTRODUCTION

In biology, mammalian sound perception is highly developed and enables mammals to recognize sound in a large dynamical range. Particularly, mammalian sound perception is able to operate in both noisy and noiseless environments with great success. For instance, signals can be reconstructed from noise corrupted data, if the signal is strong enough. This effect is called cocktail party effect (Cherry, 1953). In particular, this remarkable dynamics are induced by a frequency selective, compressive nonlinearity in the cochlea (Eguíluz et al., 2000). The principles of this dynamics are explained subsequently by summarizing the anatomy and physiology of the cochlea, see, e.g., Saladin and Miller (1998):

The cochlea consists of three coiled tubes. The most significant processing is performed in the scala media and the scala tympani. These are separated by the basilar membrane, which has a fixed end connected to the middle ear and a free end at the end of the tubes. Moreover, inner and outer hair cells are placed on the basilar membrane inside the scala media. The inner hair cells transform mechanical signals into electric signals, while the outer hair cells are used to control the oscillations of the inner hair cells by using an additional membrane, the so-called tectorial membrane, to attenuate or to amplify the mechanical signal. Hence, an acoustic signal is transduced and processed by first decomposing the signal into its different frequency components by the basilar membrane. This is possible, since the stiffness and shape of the basilar membrane is changing over space. Then these frequency components are transformed into an electrical signal by the inner hair cells. Herein, the gain of the inner hair cells is controlled by the interplay between the outer hair cells and the tectorial membrane resulting in an adaptive processing of the acoustic signal. This is controlled by motor nerve cells inside of the outer hair cells.

Even though state of the art technical sound processing has improved substantially by implementing nonlinearities in the signal pre-processing and using artificial neural networks for recognition (Abreu Araujo et al., 2020; Abeßer, 2020; Wu et al., 2020), the achieved performance still lags behind mammalian sound perception. This comes from the fact that the pre-processing is not implemented within the sensor. To improve performance, a neuromorphic microphone could be used (Smith, 2015). This kind of microphone is supposed to mimic the frequency selective and compressive nonlinearity of the sound perception by using a feedback loop. Subsequently, it is assumed that this feedback loop controls an Andronov-Hopf bifurcation, since this bifurcation is assumed to be responsible for the remarkable behavior of the cochlea (Kern and Stoop, 2003). Neuromorphic microphones can be realized using microelectromechanical (MEMS) sensors, such as those considered in Lenk et al. (2018, 2020, 2023) which are composed of thermally actuated cantilevers, where the deflection is measured by a piezo-electric layer. It has been shown that by feeding back the velocity accordingly, two Andronov-Hopf bifurcations with a constant resonance frequency are induced (Lenk et al., 2018, 2023; Rolf and Meurer, 2023). However, this constant resonance frequency is disadvantageous for this kind of systems, since the Andronov-Hopf bifurcation is frequency selective, such that many MEMS sensors are needed to construct a microphone. This disadvantage can be resolved by enabling tunability of the resonance frequency of the MEMS sensor.

[1] Funded by the Deutsche Forschungsgemeinschaft (DFG, German Research Foundation) – Project-ID 434434223 – SFB 1461.

10.1016/j.ifacol.2024.07.065

This can be achieved, e.g., by introducing a geometric nonlinearity (Asadi et al., 2017).

In this work, a T-shaped MEMS sensor is modeled and analyzed. This is done by separately modeling the mechanical and thermodynamic dynamics of the MEMS sensor. Note that the geometry of this sensor is depicted in Figure 1 and it is shown subsequently that this geometry introduces a geometric nonlinearity in the mechanical subsystem, so that this subsystem can be described by the Duffing equation. This implies in comparison to cantilever designs that the T-shaped MEMS sensor has a tunable resonance frequency in terms of the pre-deflection. Moreover, the critical point of the saddle-node bifurcation for a harmonically excited MEMS sensor is approximated by analyzing the polynomial discriminant of its steady state.

The remainder of the paper is structured as follows: The model of the MEMS sensor is summarized in Section 2. Here, a dominant mode model is considered by applying the Rayleigh-Ritz method on the mechanical system and the Galerkin method on the thermodynamic system. In Section 3 the unexcited, T-shaped MEMS sensor is analyzed with respect to its tunable resonance frequency and emerging Andronov-Hopf bifurcations. The orbits of a harmonically excited sensor are investigated in Section 4. Here, the feedback of the system is neglected and the required amplitudes and frequencies of the external signal to achieve multiple stable orbits are analyzed analytically. Final remarks in Section 5 conclude the paper.

2. MATHEMATICAL MODEL

In the following, the derivation of the dominant mode model of the MEMS sensor with a T-shaped geometry is briefly summarized. The sensor configuration is schematically depicted in Figure 1. The MEMS sensor consists of three layers, where the material of each layer is assumed homogeneous and isotropic. Particularly, the geometry can be reduced to a cantilever coupled to a clamped beam after applying the free-body principle (Reddy, 2017). By doing this, the interaction between the beams is given by a force, which is applied at the interconnection of both beams. In addition, the beams are assumed to have rectangular cross-section with the cantilever being actuated thermally by applying a controllable voltage to the aluminum layer. With these considerations, the model of this sensor is derived by dividing this system into a mechanical and thermodynamic subsystem.

The model of the mechanical subsystem is derived by applying Hamilton's principle (Reddy, 2017). Here the

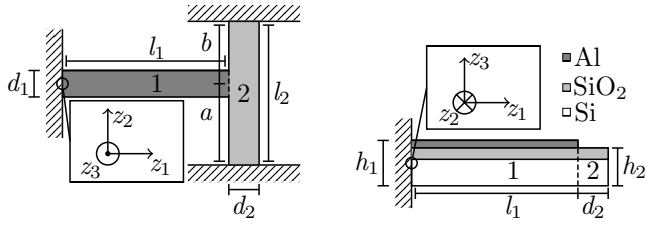

(a) Sketch of the MEMS sensor in the $z_1\,z_2$-plane.

(b) Sketch of the MEMS sensor in the $z_1\,z_3$-plane.

Fig. 1. Sketch of the mechanical subsystem of the T-shaped MEMS sensor.

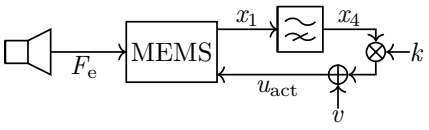

Fig. 2. Bio-inspired setup of the T-shaped MEMS sensor.

considered mechanical subsystem is only the cantilever, which is modeled by an Euler-Bernoulli beam with an additional external force. Note that the force acts on the tip and that it is not necessarily parallel to the direction of movement of the tip. For small deflections, the corresponding force contribution can be approximated by

$$F_\perp = cw_3\cos(\varphi) \approx cw_3 + \tfrac{c}{2l_1^2}\,w_3^3,$$

with the deflection $w_3(t) \in \mathbb{R}$ in z_3-direction and the spring constant $c > 0$. Herein, the angle and the cosine are approximated by $\varphi \approx w_3/l_1$ and a Taylor series approximation, such that the clamped beam can be interpreted as a nonlinear spring attached to the free end of a cantilever. Moreover, the mechanical and thermodynamic subsystems are coupled with the Duhamel-Neumann law (Nowacki et al., 1977) and it is assumed that the mechanical subsystem has linear friction.

To control the MEMS sensor, a thermal actuator is used to change the pre-deflection and gain of this sensor. Particularly, the thermal actuator can change the elasticity of the sensor, since the sensor has three layers with different moments of area. Hence, the thermodynamic subsystem is described by the linearization of the generalized heat conduction of thermoelasticity (Nowacki et al., 1977). Herein, the boundary conditions are given by the interaction between the MEMS sensor and its environment. The boundary condition of the tip is assumed to be adiabatic since the heat transfer between the tip and air is negligible. In contrast to this, the boundary condition of the clamped end is assumed to be isothermal, since it is connected to a silicon wafer. This comes from the fact that the wafer is much larger than the MEMS sensor, so that the heat conducted from the sensor to the wafer cannot heat the wafer effectively resulting in a constant temperature.

With these considerations, the dominant mode model of the T-shaped MEMS sensor is derived by applying the Rayleigh-Ritz method on the mechanical subsystem and the Galerkin method on the thermodynamic subsystem (Reddy, 2017). Subsequently, only the first mode of the dominant mode model is considered, since the higher modes are not excited by an acoustic signal. This comes from the fact that the maximum frequency of an acoustic signal is too small to excite higher modes. In view of a practical realization the system is extended by a high pass to remove the offset in the feedback. This realization is sketched in Figure 2. With these considerations, the dominant mode model is described as follows

$$\frac{\mathrm{d}}{\mathrm{d}t}\begin{bmatrix} x_1 \\ x_2 \\ x_3 \\ x_4 \end{bmatrix} = \overbrace{\begin{bmatrix} x_2 \\ -c_1x_1 - c_3x_1^3 - \mu x_2 + \alpha x_3 + \frac{1}{m}F_\mathrm{e} \\ -\beta x_3 + \zeta(kx_4 + v)^2 \\ -\frac{1}{\tau}x_4 + \kappa x_2 \end{bmatrix}}^{=\boldsymbol{f}(\boldsymbol{x},\boldsymbol{u})}, \qquad (1)$$
$$t > 0, \quad \boldsymbol{x}(0) = \boldsymbol{x}_0$$

with the state vector $\boldsymbol{x}(t) = [x_1(t)\ x_2(t)\ x_3(t)\ x_4(t)]^{\mathrm{T}} \in \mathbb{R}^4$, the input vector $\boldsymbol{u}(t) = [F_{\mathrm{e}}(t)\ v(t)]^{\mathrm{T}} \in \mathbb{R}^2$, and initial conditions $\boldsymbol{x}_0 \in \mathbb{R}^4$. The state vector and input vector are composed of the deflection $x_1(t)$, the velocity $x_2(t)$, the temperature $x_3(t)$, the output of the high pass filter $x_4(t)$, thermal input $v(t)$, and the external input $F_{\mathrm{e}}(t)$. Parameters are given by the spring constants $c_1, c_3 > 0$, the damping coefficient $\mu > 0$, the Q-factor $Q_0 > 0$, the transfer factors $\zeta = \gamma/R^2 > 0$, $\alpha, \gamma > 0$, the time constants $\beta, \tau > 0$, the mass $m > 0$, the resistance $R > 0$, the calibration factor $\kappa > 0$, and the feedback strength $k \in \mathbb{R}$.

3. BIFURCATION ANALYSIS

Subsequently, the bifurcations of the dominant mode model of the T-shaped MEMS sensor without harmonic excitation are analyzed, i.e., $v(t) = u_{\mathrm{DC}} \in \mathbb{R}$ and $F_{\mathrm{e}}(t) = 0$. Additionally, the results are verified numerically. For this, the parameters in Table A.1 are used.

The equilibria of the T-shaped MEMS sensor are analyzed first, since a saddle-node bifurcation induced by the Duffing equation might emerge with respect to u_{DC} and k.

Lemma 1. The T-shaped MEMS sensor has a unique real-valued equilibrium given by

$$\boldsymbol{x}_{\mathrm{eq}} = \left[\sqrt{\frac{4p}{3}}\sinh\left(\frac{1}{3}\operatorname{arsinh}\left(\frac{q}{2}\sqrt[3]{\frac{3}{p}}\right)\right)\ 0\ \frac{\zeta}{\beta}u_{\mathrm{DC}}^2\ 0\right]^{\mathrm{T}} \tag{2}$$

with the coefficients $p = \frac{c_1}{c_3}$, $q = -\frac{\alpha\zeta}{\beta c_3}u_{\mathrm{DC}}^2$, and the DC-voltage $u_{\mathrm{DC}} \in \mathbb{R}$.

Proof. Let the equilibria of the states and the thermal input be denoted by $\boldsymbol{x}_{\mathrm{eq}} \in \mathbb{R}^4$ $u_{\mathrm{DC}} \in \mathbb{R}$. To determine the equilibria of (1), the rate of change of the equilibria must be zero, i.e., $\dot{\boldsymbol{x}}_{\mathrm{eq}} = 0$. This implies that equilibria $\boldsymbol{x}_{\mathrm{eq}}$ are derived by solving

$$0 = x_2, \tag{3a}$$
$$0 = -c_1x_1 - c_3x_1^3 - \mu x_2 + \alpha x_3, \tag{3b}$$
$$0 = -\beta x_3 + \zeta(kx_4 + u_{\mathrm{DC}})^2, \tag{3c}$$
$$0 = -\tfrac{1}{\tau}x_4 + \kappa x_2. \tag{3d}$$

From (3a), (3c) and (3d) the equilibrium values $x_{2,\mathrm{eq}}$, $x_{3,\mathrm{eq}}$ and $x_{4,\mathrm{eq}}$ follow. After inserting these solutions into (3b), a cubic polynomial is derived. This is given by

$$P(x_{1,\mathrm{eq}}) = x_{1,\mathrm{eq}}^3 + px_{1,\mathrm{eq}} - q.$$

with the coefficients $p = \frac{c_1}{c_3}$ and $q = \frac{\alpha\zeta}{\beta c_3}u_{\mathrm{DC}}^2$. In particular, the equilibrium values have to be real. Thus the number of real solutions of the equilibria are derived. This is done by analyzing the polynomial discriminant $D_{\mathrm{eq}} = (p/3)^3 + (q/2)^2$. Then the number of real zeros of a cubic polynomial are determined following Nickalls (1993)

$$D_{\mathrm{eq}}\begin{cases} > 0, & P \text{ has 1 real root,} \\ = 0, & P \text{ has 3 real roots and 2 roots are equal,} \\ < 0, & P \text{ has 3 different, real roots.} \end{cases}$$

Inserting p and q into the polynomial discriminant yields

$$D_{\mathrm{eq}} = \frac{c_1^3}{c_3^3} + \frac{\alpha^2\zeta^2}{\beta^2 c_3^2}u_{\mathrm{DC}}^4 > 0.$$

Hence, (1) has an unique real-valued equilibrium. Additionally, the equilibrium of the deflection is determined by the sinh-solution of a cubic equation, since $p > 0$ (Holmes, 2002). This yields the equilibrium values of $x_{1,\mathrm{eq}}$ and concludes the proof. □

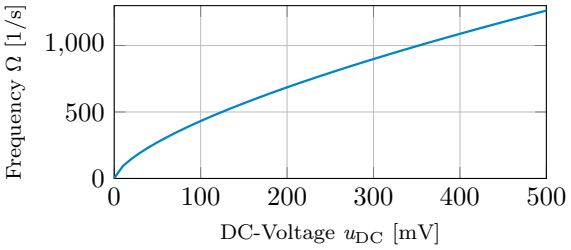

Fig. 3. Natural frequency Ω of T-shaped MEMS sensor in terms of the DC-voltage u_{DC}.

Particularly, the T-shaped MEMS sensor given by (1) does not experience a saddle-node bifurcation induced by the feedback strength k and the DC-voltage u_{DC}, since it has a unique real-valued equilibrium in this case. This changes if the MEMS sensor is excited by a harmonic input (Holmes and Rand, 1976; Guckenheimer and Holmes, 2013). Its critical points are investigated in the subsequent section for the dominant mode model without feedback, i.e., $k = 0$. To conclude this section, the existence of an Andronov-Hopf bifurcation is analyzed. In general the linearization of (1) is given by

$$\Delta\dot{\boldsymbol{x}} = A\Delta\boldsymbol{x} + B\Delta\boldsymbol{u}$$

with the error states $\Delta\boldsymbol{x}(t) = \boldsymbol{x}(t) - \boldsymbol{x}_{\mathrm{eq}} \in \mathbb{R}^4$ and the shifted inputs $\Delta\boldsymbol{u}(t) = \boldsymbol{u}(t) - \boldsymbol{u}_{\mathrm{eq}} \in \mathbb{R}^2$. The system matrix $A \in \mathbb{R}^{4\times4}$ and the input matrix $B \in \mathbb{R}^{4\times2}$ are given by

$$A = \frac{\partial \boldsymbol{f}}{\partial \boldsymbol{x}}(\boldsymbol{x}_{\mathrm{eq}}, \boldsymbol{u}_{\mathrm{eq}}) = \begin{bmatrix} 0 & 1 & 0 & 0 \\ -\Omega^2 & -\mu & \alpha & 0 \\ 0 & 0 & -\beta & 2\zeta u_{\mathrm{DC}}k \\ 0 & \kappa & 0 & -1/\tau \end{bmatrix}, \tag{4a}$$

$$B = \frac{\partial \boldsymbol{f}}{\partial \boldsymbol{u}}(\boldsymbol{x}_{\mathrm{eq}}, \boldsymbol{u}_{\mathrm{eq}}) = \begin{bmatrix} 0 & 1/m & 0 & 0 \\ 0 & 0 & \zeta & 0 \end{bmatrix}^{\mathrm{T}} \tag{4b}$$

with the natural frequency $\Omega = (c_1 + 3c_3x_{1,\mathrm{eq}}^2)^{1/2}$.

Remark 2. (Frequency Tunability). It should be noted that the natural frequency Ω depends on the equilibrium $x_{1,\mathrm{eq}}$. This implies that the natural frequency Ω can be controlled by applying the DC-voltage u_{DC} accordingly. This property is called tunability and a numerical illustration is presented in Figure 3.

The T-shaped MEMS sensor has two Andronov-Hopf bifurcations. This comes from the fact, that compared to the cantilevered MEMS sensor investigated in Lenk et al. (2023); Rolf and Meurer (2023), the system matrix of the linearization is not changed structurally by introducing the cubic term. The following theorem gives further insight in the emergence of the Andronov-Hopf bifurcations.

Theorem 3. Let the feedback strength k be the bifurcation parameter. Then the system (1) undergoes two Andronov-Hopf bifurcations with the critical points $k_{\mathrm{H}}^{\pm}$ and respective resonance frequencies $\omega_{\mathrm{R}}^{\pm}$ given by (5).

Proof. Formally, the emergence of an Andronov-Hopf bifurcation is shown by using the Hopf Theorem in $\mathbb{R}^N$,

$$k_{\mathrm{H}}^{\pm} = -\frac{1}{4\alpha\zeta\kappa\tau^2 u_{\mathrm{DC}}}\Big[\mu\tau\left(\beta^2\tau+\beta+\tau\Omega^2\right)+\mu+(\beta\tau+1)\left(\mu^2\tau+\beta-\tau\Omega^2\right) \pm(\mu\tau+\beta\tau+1)\sqrt{(\beta\mu\tau+\beta+\mu+\tau\Omega^2)^2-4\beta\tau\Omega^2}\Big] \tag{5a}$$

$$\omega_{\mathrm{H}}^{\pm} = \sqrt{\frac{(\beta\mu+\Omega^2)\,\tau+\beta+\mu\pm\sqrt{\left[(\beta\mu+\Omega^2)\,\tau+\beta+\mu\right]^2-4\beta\tau\Omega^2}}{2\tau}} \tag{5b}$$

see, e.g., Guckenheimer and Holmes (2013). However, the local analysis of (1), i.e., the analysis of the eigenvalues of the system matrix A, can be omitted, since A given by (4a) is structurally equivalent to the system matrix of the cantilevered sensor (Rolf and Meurer, 2023). □

Remark 4. In particular, the simulations of the dominant mode model of the T-shaped MEMS sensor indicate that the limit cycles in the super-critical are asymptotically stable. Note that the limit cycles of $[x_1\ x_2\ x_3]^{\mathrm{T}}$ are shown in Figure 4. The stabilization might be caused by the cubic term in $\dot{x}_2$, which is introduced by the geometric nonlinearity, since the spring constant c_3 is assumed to be positive.

4. ANALYSIS OF EMERGING ORBITS

Subsequently, the critical points of the saddle-node bifurcations for the uncontrolled case, i.e., $k = 0$, are investigated analytically. Note that the existence of the saddle-node bifurcation is already shown and evaluated numerically in Holmes and Rand (1976); Guckenheimer and Holmes (2013) for this cases. Yet, to the best of our knowledge the critical points of these saddle-node bifurcations have not been approximated by analyzing the polynomial discriminant of the equilibrium of the averaged system. Henceforth, the analysis is done by approximating the Poincare map with the Averaging Theorem, see, e.g., (Guckenheimer and Holmes, 2013, Theorem 4.1.1). For this it is assumed that the inputs are given by

$$v(t) = u_{\mathrm{DC}} + u_{\mathrm{AC}}\cos(\omega_{\mathrm{e}}t+\varphi_{\mathrm{AC}}), \tag{6a}$$
$$F_{\mathrm{e}}(t) = r_{\mathrm{e}}\sin(\omega_{\mathrm{e}}t+\varphi_{\mathrm{e}}) \tag{6b}$$

with the amplitudes $r_{\mathrm{e}}, u_{\mathrm{AC}} > 0$, the DC-voltage $u_{\mathrm{DC}} \in \mathbb{R}$, the frequency $\omega_{\mathrm{e}} > 0$, and the phases $\varphi_{\mathrm{e}}, \varphi_{\mathrm{AC}} \in [0, 2\pi)$. Note that the assumption (6a) on the external input F_{e} can be interpreted as an acoustic signal. In contrast to this, the thermal input v can be interpreted as a (generalized) closed loop signal, since feedback results also approximately in a harmonic oscillation, which is constrained by the external inputs F_{e} and the parameters of the sensors.

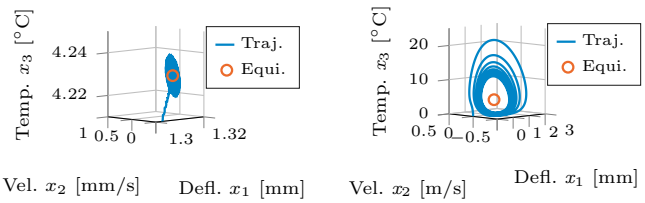

(a) After surpassing k_{H}^{+}. (b) After surpassing k_{H}^{-}.

Fig. 4. Limit cycles of $[x_1\ x_2\ x_3]^{\mathrm{T}}$ after surpassing the critical points. Note that the feedback strength is given by $k \in \{1.1\times k_{\mathrm{H}}^{+}, 1.1\times k_{\mathrm{H}}^{-}\}$.

Hence, the amplitude u_{AC} can be interpreted as a function of the feedback strength k, the input F_{e}, and DC-voltage u_{DC}.

Assuming $k = 0$, it follows that the thermal and mechanical subsystem are cascaded. Then the steady state of the thermal subsystem is given by

$$x_3(t) = \bar{r} + \tilde{r}_1\cos(\omega_{\mathrm{e},1}t-\varphi_{\mathrm{e},2}) + \tilde{r}_2\cos(2\omega_{\mathrm{e}}t-\varphi_{\mathrm{e},1})$$

with the phases $\varphi_{\mathrm{e},1} = \varphi_{\mathrm{AC}} + \arctan(\omega_{\mathrm{e}}/\beta)$ and $\varphi_{\mathrm{e},2} = \varphi_{\mathrm{AC}}+\arctan(2\omega_{\mathrm{e}}/\beta)$, and the amplitudes $\bar{r} = \frac{\alpha\zeta(2u_{\mathrm{DC}}^2+u_{\mathrm{AC}}^2)}{2\beta}$, $\tilde{r}_1 = \frac{\zeta u_{\mathrm{AC}}u_{\mathrm{DC}}}{\sqrt{\beta^2+\omega_{\mathrm{e}}^2}}$ and $\tilde{r}_2 = \frac{\zeta u_{\mathrm{AC}}^2}{2\sqrt{\beta^2+4\omega_{\mathrm{e}}^2}}$. After inserting the steady state response of the thermal subsystem into the mechanical subsystem, a harmonically excited Duffing oscillator emerges. This is governed by

$$\dot{x}_1 = x_2, \tag{7a}$$
$$\dot{x}_2 = -c_1x_1 - \mu x_2 - c_3x_1^3 + \bar{r} + \tilde{r}\cos(\omega_{\mathrm{e}}t-\varphi_{\mathrm{e},1}) + \tilde{r}_2\cos(2\omega_{\mathrm{e}}t-\varphi_{\mathrm{e},2}) \tag{7b}$$

with the amplitude $\tilde{r} = \tilde{r}_1 + r_{\mathrm{e}}/m$. With these preliminaries, the results on the critical points of the saddle-node bifurcation are stated subsequently.

Theorem 5. Let the feedback strength be $k = 0$ and assume that the thermal actuator and the external input are given by (6). Additionally, denote the bifurcation parameters by $\tilde{r} > 0$ and $\omega_{\mathrm{e}} > 0$. Then the MEMS sensor given by (1) undergoes two saddle-node bifurcations, if the external frequency is in a neighborhood of $\mathcal{I}_{\omega_{\mathrm{SN}}}^{+} = [\omega_{\mathrm{SN}}, \infty)$ and the external amplitude is in a neighborhood of the critical amplitudes $\tilde{r}_{\mathrm{SN}}^{\pm}$ with the critical points

$$\omega_{\mathrm{SN}} = \frac{\sqrt{2}}{2}\sqrt{3\mu^2+2\Omega^2+\mu\sqrt{9\mu^2+12\Omega^2}}, \tag{8a}$$
$$\tilde{r}_{\mathrm{SN}}^{\pm} = \frac{2}{9}\sqrt{\frac{2}{c_3}}\sqrt{-\Omega_\Delta^6 - 9\mu^2\Omega_\Delta^2\omega_{\mathrm{e}}^2 \pm \left(\Omega_\Delta^4 - 3\mu^2\omega_{\mathrm{e}}^2\right)^{\frac{3}{2}}} \tag{8b}$$

and $\tilde{r}_{\mathrm{SN}}^{+} > \tilde{r}_{\mathrm{SN}}^{-} > 0$. Here, the frequency difference is given by $\Omega_\Delta^2 = \Omega^2 - \omega_{\mathrm{e}}^2$. Moreover, there are two stable orbits and one unstable orbit, if $\tilde{r} \in \mathcal{I}_{\tilde{r}_{\mathrm{SN}}} = (\tilde{r}_{\mathrm{SN}}^{-}, \tilde{r}_{\mathrm{SN}}^{+})$ and $\omega_{\mathrm{e}} \in \mathcal{I}_{\omega_{\mathrm{SN}}}$.

Remark 6. The feedback strength k influences mostly the damping coefficient μ and the natural frequency Ω, if $u_{\mathrm{DC}}k < 0$ holds true. In this case the MEMS sensor with feedback can be approximated by replacing the damping coefficient μ with the effective damping $\mu_{\mathrm{eff}}(k)$ with $0 \le \mu_{\mathrm{eff}}(k) \le \mu$ and adding an additional component u_{AC}^2 to u_{DC}^2. In particular, the shift of the DC-voltage implies a change in the natural frequency, which is dependent on the (unknown) external excitation.

Proof. The main idea of this proof is based on (Guckenheimer and Holmes, 2013, Theorem 4.3.1), which states that, if the averaged system has a saddle-node bifurcation at the critical point $\mu^* \in \mathbb{R}$, the Poincare map of the

original system also has a saddle-node bifurcation in a neighborhood of μ^*. Hence, the proof is structured as follows: First, (7) is transformed, so that the Averaging Theorem can be applied and its equilibria can be analyzed. Then, the number of real equilibria are investigated. This is done with the polynomial discriminant, since the equilibrium condition can be expressed by a cubic equation. Finally, the properties of the original system are discussed.

Before using the Averaging Theorem, the equilibrium of (7) is moved into the origin. This is done by introducing difference coordinates $\Delta\boldsymbol{x} = \boldsymbol{x} - \boldsymbol{x}_{\mathrm{eq}}$ with the equilibrium $\boldsymbol{x}_{\mathrm{eq}}$ structurally given by (2)[2]. Then the oscillator is governed by

$$\begin{aligned}\Delta\dot{x}_1 =&\Delta x_2,\\ \Delta\dot{x}_2 =&-\Omega^2\Delta x_1 - \mu\Delta x_2 - 3c_3 x_{1,\mathrm{eq}}\Delta x_1^2 - c_3\Delta x_1^3\\ &+\tilde{r}\cos(\omega_{\mathrm{e}}t-\varphi_{\mathrm{e},1}) + \tilde{r}_2\cos(2\omega_{\mathrm{e}}t-\varphi_{\mathrm{e},2}).\end{aligned}$$

After that, the Averaging Theorem can be used by applying the Van-der-Pol transformation (Guckenheimer and Holmes, 2013)

$$\begin{bmatrix}w_1\\ w_2\end{bmatrix} = \begin{bmatrix}\cos(\omega_{\mathrm{e}}t+\varphi_{\mathrm{e}}) & -\sin(\omega_{\mathrm{e}}t+\varphi_{\mathrm{e}})/\omega_{\mathrm{e}}\\ -\sin(\omega_{\mathrm{e}}t+\varphi_{\mathrm{e}}) & -\cos(\omega_{\mathrm{e}}t+\varphi_{\mathrm{e}})/\omega_{\mathrm{e}}\end{bmatrix}\begin{bmatrix}\Delta x_1\\ \Delta x_2\end{bmatrix}.$$

This yields

$$\dot{w}_1 = -\tfrac{\mu}{2}w_1 - \tfrac{\Omega_\Delta^2}{2\omega_{\mathrm{e}}}w_2 - \tfrac{3c_3}{8\omega_{\mathrm{e}}}(w_1^2+w_2^2)w_2, \tag{9a}$$

$$\dot{w}_2 = \tfrac{\Omega_\Delta^2}{2\omega_{\mathrm{e}}}w_1 - \tfrac{\mu}{2}w_2 + \tfrac{3c_3}{8\omega_{\mathrm{e}}}(w_1^2+w_2^2)w_1 - \tfrac{\tilde{r}}{2\omega_{\mathrm{e}}} \tag{9b}$$

with the frequency difference $\Omega_\Delta^2 = \Omega^2 - \omega_{\mathrm{e}}^2$. The orbits of (7) are derived by computing the equilibria of the polar coordinates of the averaged system (9). Using the transformation to the polar coordinates, i.e., $\rho^2 = w_1^2 + w_2^2$ and $\tan(\phi) = w_2/w_1$, yields

$$\dot{\rho} = -\tfrac{\mu}{2}\rho - \tfrac{\tilde{r}}{2\omega_{\mathrm{e}}}\sin(\phi), \quad \rho\dot{\phi} = \tfrac{\Omega_\Delta^2}{2\omega_{\mathrm{e}}}\rho + \tfrac{3c_3}{8\omega_{\mathrm{e}}}\rho^3 - \tfrac{\tilde{r}}{2\omega_{\mathrm{e}}}\cos(\phi).$$

By inserting $\dot{\rho} = 0$, $\dot{\phi} = 0$, dividing by $9c_3^2/64\omega_{\mathrm{e}}$ and rearranging the equations, the equilibria are given by

$$\phi_{\mathrm{eq}} \in \{-\varphi + 2\pi c_1,\ \varphi + \pi + 2\pi c_1\}, \tag{10a}$$

$$0 = x^3 + \tfrac{24\Omega_\Delta^2}{9c_3}x^2 + \tfrac{16\left(\Omega_\Delta^4 - \omega_{\mathrm{e}}^2\mu^2\right)}{9c_3^2}x - \tfrac{16\tilde{r}^2}{9c_3^2}. \tag{10b}$$

with the phase $\varphi = \arcsin(\tfrac{\omega_{\mathrm{e}}\mu}{\tilde{r}}\rho_{\mathrm{eq}})$, the constant $c_1 \in \mathbb{Z}$ and variable $x = \rho_{\mathrm{eq}}^2$. Note that the phase has real-valued solutions, if $|\omega_{\mathrm{e}}\mu\rho_{\mathrm{eq}}| < \tilde{r}$ is satisfied. By substituting $y = x + \frac{24\Omega_\Delta^2}{27c_3}$, (10b) is transformed into a depressed cubic, i.e., $y^3 + p_\rho y - q_\rho$. Herein the coefficients are given by

$$p_\rho = \tfrac{16\left(3\mu^2\omega_{\mathrm{e}}^2 - \Omega_\Delta^4\right)}{27c_3^2}, \quad q_\rho = \tfrac{16\left(81c_3r^2 + 8\left(\Omega_\Delta^6 + 9\mu^2\Omega_\Delta^2\omega_{\mathrm{e}}^2\right)\right)}{729c_3^3}.$$

Particularly, the number of real solutions of (10b) can be determined by analyzing the polynomial discriminant $D_\rho(\tilde{r}_{\mathrm{SN}}, \omega_{\mathrm{SN}}) = p_\rho^3/27 + q_\rho^2/4 = 0$. Here the bifurcation parameters of the saddle-node bifurcation are denoted by $\tilde{r} > 0$ and $\omega_{\mathrm{e}} > 0$. By rearranging D_ρ with respect to $\tilde{r}$, a biquadratic polynomial arises, i.e., $D_\rho(\tilde{r}, \omega_{\mathrm{e}}) = \tilde{r}^4 + a_2(\omega_{\mathrm{e}})\tilde{r}^2 + a_0(\omega_{\mathrm{e}})$ with

$$a_2 = \tfrac{16\left(\Omega_\Delta^6 + 9\mu^2\Omega_\Delta^2\omega_{\mathrm{e}}^2\right)}{81c_3}, \qquad a_0 = \tfrac{64\mu^2\omega_{\mathrm{e}}^2\left(\Omega_\Delta^4 + \mu^2\omega_{\mathrm{e}}^2\right)^2}{243c_3^2}.$$

The critical points are given by the roots of this biquadratic polynomial. This yields (8b) with the critical amplitudes $\tilde{r}_{\mathrm{SN}}^+ > \tilde{r}_{\mathrm{SN}}^- > 0$. Notably, the polynomial discriminant D_ρ is always positive, if the amplitude $\tilde{r}$ is large enough. Only if the amplitude $\tilde{r}$ is inside the interval $\mathcal{I}_{\tilde{r}_{\mathrm{SN}}} = [\tilde{r}_{\mathrm{SN}}^-, \tilde{r}_{\mathrm{SN}}^+]$, the polynomial discriminant satisfies $D_\rho \leq 0$. Moreover, the solution for $D_\rho = 0$ might become imaginary. This is analyzed with respect to the external frequency subsequently. After inserting $\Omega_\Delta^2 = \Omega^2 - \omega_{\mathrm{e}}^2$ into (8b) and investigating the square root and non-square root term independently, the conditions, implying that the amplitudes $\tilde{r}_{\mathrm{SN}}^\pm$ are real-valued, are given by

$$0 \leq \omega_{\mathrm{e}}^4 + b_2\omega_{\mathrm{e}}^2 + b_0, \tag{11a}$$

$$0 \leq \omega_{\mathrm{e}}^6 + (9\mu^2 - 3\Omega^2)\omega_{\mathrm{e}}^4 + (3\Omega^4 - 9\mu^2\Omega^2)\omega_{\mathrm{e}}^2 - \Omega^6 \tag{11b}$$

with the coefficients $b_2 = -\left(3\mu^2 - 2\Omega^2\right)$ and $b_0 = \Omega^4$. Particularly, (11a) has two roots

$$\omega_{\mathrm{SN}}^\pm = \tfrac{\sqrt{2}}{2}\sqrt{3\mu^2 + 2\Omega^2 \pm \mu\sqrt{9\mu^2 + 12\Omega^2}} \tag{12}$$

with the critical points $\omega_{\mathrm{SN}}^+ > \omega_{\mathrm{SN}}^- > 0$. Furthermore, it is possible to compute with (12) the intervals in which (11a) is satisfied. These intervals are given by $\mathcal{I}_{\omega_{\mathrm{SN}}}^- = (0, \omega_{\mathrm{SN}}^-]$ and $\mathcal{I}_{\omega_{\mathrm{SN}}}^+ = [\omega_{\mathrm{SN}}^+, \infty)$, since the coefficients $b_0 > 0$. Thus, (11b) has to be satisfied either on $\mathcal{I}_{\omega_{\mathrm{SN}}}^-$ or $\mathcal{I}_{\omega_{\mathrm{SN}}}^+$. Inserting (12) into (11b), yields the condition

$$\pm\left(3\mu^2 + \Omega^2\right)\sqrt{9\mu^2 + 12\Omega^2} \leq 9\mu\left(\mu^2 + \Omega^2\right). \tag{13}$$

In fact, (13) is only violated on $\mathcal{I}_{\omega_{\mathrm{SN}}}^+$, since it can be reduced to $\mu \geq 0$ and $\Omega = 0$. Hence, it can be concluded with the Implicit Function Theorem that the critical amplitudes $\tilde{r}_{\mathrm{SN}}^\pm$ with an external frequency $\omega_{\mathrm{e}} \in \mathcal{I}_{\omega_{\mathrm{SN}}}^+$ induce two bifurcations in (9), since the change of the number of equilibria imply a rank loss of the Jacobian, such that the original system is going to have also two bifurcations in the neighborhood of these critical points. Indeed it can be concluded from (Guckenheimer and Holmes, 2013, Chapter 4.3) that these two bifurcations

[2] Note that exact equilibrium value changes in comparison to the equilibrium of the unexcited system, since the offset changes by introducing a harmonic oscillation in the thermal input $v(t)$.

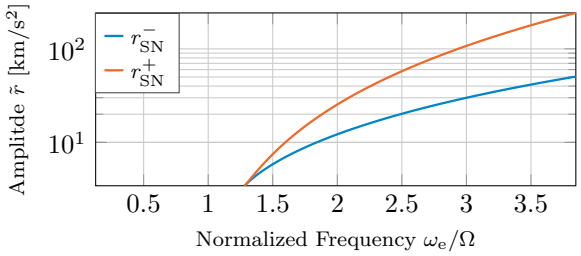

(a) Critical amplitude $\tilde{r}_{\mathrm{SN}}$ of the T-shaped MEMS sensor in terms of normalized frequency ω/Ω.

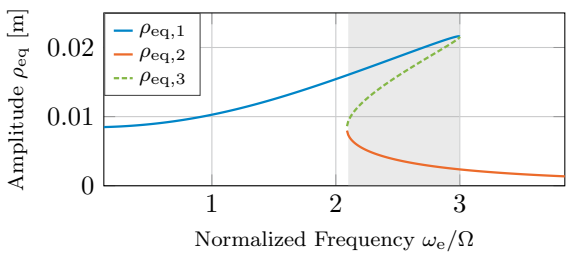

(b) Frequency response of the T-shaped MEMS sensor with an excitation amplitude $\tilde{r} = 30\ \frac{\mathrm{km}}{\mathrm{s}^2}$.

Fig. 5. Critical amplitude and frequency response of the T-shaped MEMS sensor.

are saddle-node bifurcations. Additionally, it follows from Holmes and Rand (1976) that (i) there is one stable equilibrium, if there is a real-valued equilibrium, (ii) there is one stable and one degenerate equilibrium, if there are two real-valued equilibrium and (iii) there are two stable equilibria and one saddle point, if there are three real-valued equilibria, where the saddle point is in between the two stable equilibria. □

For illustration purposes, the orbits with a DC-voltage $u_{\mathrm{DC}} = -0.5\,\mathrm{V}$ and amplitude $\tilde{r} = 30\,\frac{\mathrm{km}}{\mathrm{s}^2}$ are analyzed numerically with the parameters given by Table A.1. In particular, the natural frequency of this MEMS sensor is given by $\Omega = 1.26\,\frac{1}{\mathrm{ms}}$. The result is shown in Figure 5 in terms of the normalized frequency $\omega_{\mathrm{e}}/\Omega$. Herein, Figure 5a depicts the critical amplitudes $\tilde{r}^{\pm}_{\mathrm{SN},}$. These critical amplitudes emerge after surpassing the critical frequency $\omega_{\mathrm{SN}} = 1.28\,\Omega$. Moreover, the saddle-node bifurcation is shown in Figure 5b. Here, the gray area depicts the interval $\mathcal{I}_{\omega_{\mathrm{SN}}} = [2.1\,\Omega, 3\,\Omega]$, in which the T-shaped MEMS sensor has possible three orbits. Note that the existence of three real-valued solutions is given, since $\rho_{\mathrm{eq}} < 30\,\mathrm{mm}$.

5. CONCLUSION

Given the T-shaped geometry of the thermally actuated MEMS sensor a dominant mode model is derived. The dominant mode model of the mechanical system is described by the Duffing equation and its thermodynamic system is described by a first order low pass with a quadratic input, respectively. The bifurcations of this system with respect to the feedback strength and external harmonic excitation are analyzed. Here, it is shown that the MEMS sensor has an Andronov-Hopf bifurcation in terms of the feedback strength and tunability is induced by exploiting the geometric nonlinearity and assigning predeflection with the thermal actuator. Moreover, the critical points of the saddle-node bifurcations are analyzed with respect to harmonic excitation by investigating the number of real-valued equilibria of the uncontrolled system. From this analysis it is concluded that after closing the control loop an external input influences the resonance frequency.

Appendix A. PARAMETERS OF THE SENSORS

The parameters of the sensor are summarized in Table A.1.

REFERENCES

Abeßer, J. (2020). A review of deep learning based methods for acoustic scene classification. *Applied Sciences*, 10(6), 2020.

Abreu Araujo, F. et al. (2020). Role of non-linear data processing on speech recognition task in the framework of reservoir computing. *Scientific reports*, 10(1), 328.

Asadi, K. et al. (2017). Mechanism of geometric nonlinearity in a nonprismatic and heterogeneous microbeam resonator. *Physical Review B*, 96(11), 115306.

Cherry, E.C. (1953). Some experiments on the recognition of speech, with one and with two ears. *The Journal of the acoustical society of America*, 25(5), 975–979.

Eguíluz, V.M., Ospeck, M., Choe, Y., Hudspeth, A.J., and Magnasco, M.O. (2000). Essential Nonlinearities in Hearing. *Physical Review Letters*, 84(22), 5232–5235.

Guckenheimer, J. and Holmes, P. (2013). *Nonlinear oscillations, dynamical systems, and bifurcations of vector fields*, volume 42. Springer Science & Business Media.

Holmes, G.C. (2002). The use of hyperbolic cosines in solving cubic polynomials. *The Mathematical Gazette*, 86(507), 473–477.

Holmes, P. and Rand, D. (1976). The bifurcations of duffing's equation: An application of catastrophe theory. *Journal of Sound and Vibration*, 44(2), 237–253.

Kern, A. and Stoop, R. (2003). Essential Role of Couplings between Hearing Nonlinearities. *Physical Review Letters*, 91(12), 128101.

Lenk, C., Ekinci, A., Rangelow, I.W., and Gutschmidt, S. (2018). Active, artificial hair cells for biomimetic sound detection based on active cantilever technology. In *2018 40th Annual International Conference of the IEEE Engineering in Medicine and Biology Society (EMBC)*, 4488–4491.

Lenk, C., Seeber, L., Ziegler, M., Hövel, P., and Gutschmidt, S. (2020). Enabling Adaptive and Enhanced Acoustic Sensing using Nonlinear Dynamics. In *2020 IEEE International Symposium on Circuits and Systems (ISCAS)*, 1–4.

Lenk, C. et al. (2023). Neuromorphic acoustic sensing using an adaptive microelectromechanical cochlea with integrated feedback. *Nature Electronics*, 1–11.

Nickalls, R. (1993). A new approach to solving the cubic: Cardan's solution revealed. *The Mathematical Gazette*, 77(480), 354–359.

Nowacki, W., Francis, P.H., Hetnarski, R.B., and Florence, A.L. (1977). Dynamic Problems of Thermoelasticity. *Journal of Applied Mechanics*, 44(2), 366–366.

Reddy, J.N. (2017). *Energy principles and variational methods in applied mechanics*. John Wiley & Sons.

Rolf, H.F.J. and Meurer, T. (2023). Amplitude control for an artificial hair cell undergoing an Andronov-Hopf bifurcation. *IFAC-PapersOnLine*, 56(1), 181–186.

Saladin, K.S. and Miller, L. (1998). *Anatomy & physiology*. WCB/McGraw-Hill New York.

Smith, L.S. (2015). Toward a neuromorphic microphone. *Frontiers in Neuroscience*, 9, 398.

Wu, J., Yılmaz, E., Zhang, M., Li, H., and Tan, K.C. (2020). Deep spiking neural networks for large vocabulary automatic speech recognition. *Frontiers in Neuroscience*, 14, 199.

Table A.1. Parameters of the simulated MEMS sensor

Parameter		Values
Spring constant	$c_1\ \left[\frac{\mathrm{N}}{\mathrm{m}}\right]$	4.88
	$c_3\ \left[\frac{\mathrm{N}}{\mathrm{m}^3}\right]$	$36.4 \cdot 10^9$
Transfer factor	$\alpha\ \left[\frac{\mathrm{m}^2}{\mathrm{Ks}^2}\right]$	19.2
	$\zeta\ \left[\frac{\mathrm{K}}{\mathrm{V}^2\mathrm{s}}\right]$	$4.2588 \cdot 10^5$
Time constant	$\beta\ \left[\frac{1}{\mathrm{s}}\right]$	$1.0066 \cdot 10^3$
	$\tau\ \left[\frac{1}{\mathrm{s}}\right]$	10^{-3}
Damping	$\mu\ \left[\frac{1}{\mathrm{s}}\right]$	366.52
Calibration	$\kappa\ \left[\frac{\mathrm{V}}{\mathrm{m}}\right]$	10^6